

# Data Driven Air Entrainment Velocity Parameterization by Breaking Waves

Xiaohui Zhou<sup>1,2</sup>, Anton S. Darmenov<sup>2</sup>, and Kianoosh Yousefi<sup>3</sup>

<sup>1</sup>Earth System Science Interdisciplinary Center, University of Maryland, College Park, MD 20740, USA

<sup>2</sup>NASA/GSFC Mail Code 610.1, Greenbelt, MD 20771

<sup>3</sup>Department of Mechanical Engineering, University of Texas at Dallas, Richardson, TX 75080, USA

## Key Points:

- Physically interpretable ML parameterization of wave-breaking air-entrainment velocity trained on 43-yr WAVEWATCH III simulations.
- ML-based  $V_a$  parameterization markedly improves on wind-only and semi-bulk schemes using wind speed and significant wave height.
- Widely available wind and wave predictors enable use across wave models, reanalyses, and observations without retraining.

## Abstract

Wave breaking injects turbulence and bubbles into the upper ocean, modulating air-sea exchange of momentum, heat, gases, and sea-spray aerosols. These fluxes depend non-linearly on sea state but remain poorly represented in coupled atmosphere-wave-ocean models, where air-entrainment velocity ( $V_a$ ) is often parameterized using wind speed or significant wave height alone. We develop a global machine-learning parameterization of  $V_a$  trained on a 43-year WAVEWATCH III simulation that resolves the breaker-front distribution  $\Lambda(c)$  and associated energetics. A multilayer perceptron with seven physically motivated predictors (wind speed, wave height, wave age, steepness, direction, and depth) reproduces spectral-reference  $V_a$  with high skill. The model reduces longstanding biases in bulk formulas, notably overestimation in swell-dominated low latitudes and underestimation in storm tracks. Applied globally, the parameterization improves estimates of bubble-mediated  $CO_2$  transfer velocity and sea-salt aerosol emission, reducing errors by roughly an order of magnitude. Validation against independent HiWinGS observations supports robust performance in deep-water, high-wind conditions.

## Plain Language Summary

Breaking waves play an important role in how the ocean exchanges gases, heat, and particles with the atmosphere. When waves break, they trap air and create bubbles that greatly increase gas exchange (such as  $CO_2$  moving into the ocean) and produce tiny sea-spray particles. Most climate models cannot explicitly simulate these breaking events, so they rely on simplified relationships based only on wind speed. These simplified formulas often produce large errors.

In this study, we use machine learning trained on decades of global wave model simulations to create a new way to estimate how much air is mixed into the ocean and sea salt emitted by breaking waves. The new method captures how wave conditions, not just wind, affect breaking. It predicts air entrainment, gas transfer, and sea salt emissions more accurately than traditional formulas. This approach can be used to improve weather forecasts, air quality studies, and long-term climate simulations by representing the ocean's whitecap processes much more realistically.

## 1 Introduction

Breaking surface waves exert a first-order control on air-sea exchanges of momentum, heat, and gases by generating intense near-surface turbulence, entraining air, and producing whitecaps and bubble plumes that enhance surface renewal and bubble-mediated transfer (e.g., Thorpe, 1995; Melville, 1996; Deane & Stokes, 2002; Melville, 2016; Ruth et al., 2022; Peláez-Zapata et al., 2024; Deike et al., 2025; Di Giorgio et al., 2025). Although whitecaps cover only a small fraction of the ocean surface, they account for a disproportionate share of wave-energy dissipation and can dominate gas transfer under moderate-to-high winds (Banner & Peirson, 2000; Callaghan & White, 2008; Sutherland & Melville, 2016; Callaghan et al., 2012). Because wave breaking is intermittent and strongly modulated by sea state (e.g., wind forcing, wave age, steepness, and swell), it remains challenging to represent consistently in coupled atmosphere-wave-ocean models and in large-scale diagnostics derived from reanalyses and wave hindcasts. As a result, many applications still rely on wind-speed-only (or semi-bulk) formulations that can miss substantial regional and regime-dependent variability associated with changes in wave development and spectral shape (Deike et al., 2017; Zhou et al., 2023).

A physically grounded framework for describing wave breaking is provided by the breaking-crest distribution  $\Lambda(c)$ , the mean length of breaking crests moving with phase speed  $c$  per unit surface area (Phillips, 1985a). Moments of  $\Lambda(c)$  connect breaking kinematics to energetics and enable sea-state-dependent estimates of dissipation and break-

ing intensity. Practical approaches to estimate  $\Lambda(c)$  in spectral wave models have made it possible to evaluate global breaking statistics and their implications for air-sea exchange in a consistent, model-based manner (Romero et al., 2012; Romero, 2019). Building on this foundation, air-entrainment velocity  $V_a$  provides a compact descriptor of breaking-driven air injection, linking wave-breaking statistics to bubble-mediated pathways that influence gas transfer and aerosol production (Deike et al., 2017). Recent implementations of  $\Lambda(c)$ -based diagnostics in WAVEWATCH III (WW3) have enabled global estimates of sea-state-dependent air entrainment and associated bubble-mediated gas fluxes (Romero, 2019; Zhou et al., 2023). However, explicitly computing  $\Lambda(c)$  and derived breaking diagnostics within operational or climate-scale workflows can be computationally expensive, and simplified parameterizations based only on wind speed can produce systematic biases (Zhou et al., 2023).

In parallel, machine learning (ML) has emerged as an effective tool for learning non-linear mappings in geophysical systems when the target quantity is well-defined and physically interpretable, and when the predictors are widely available from models or observations. ML approaches have been used across Earth system science for parameterization, emulation, and downscaling, including wave and air-sea applications where the goal is to capture sea-state dependence at low computational cost (e.g., James et al., 2018; O'Donncha et al., 2018, 2019; Lou et al., 2021; Zhang et al., 2022; Sun et al., 2022; Dakar et al., 2023; Xu et al., 2023). For wave-breaking-related quantities, a key requirement is portability: the model should be driven by predictors that are routinely available (e.g.,  $U_{10}$ ,  $H_s$ , wave age, steepness, direction, and depth) and should generalize across basins and regimes without ad hoc tuning. This motivates a surrogate approach that retains the physics embedded in the spectral,  $\Lambda(c)$ -based reference while providing an efficient diagnostic that can be evaluated everywhere that standard wind and wave fields exist.

Here we develop a data-driven, computationally inexpensive surrogate for  $V_a$  by training a multilayer perceptron (MLP) on a 43-year global WW3 hindcast in which  $\Lambda(c)$  and associated breaking energetics are diagnosed. The model uses seven physically motivated predictors (significant wave height  $H_s$ , 10-m wind speed  $U_{10}$ , wind direction, wave age  $c_p/U_{10}$ , wave steepness  $k_p H_s/2$ , and water depth) to reproduce the spectral-reference  $V_a$  with high fidelity. We evaluate performance globally using withheld years (2019–2022) and validate against independent observations from HiWinGS (Brumer et al., 2017), focusing on the ability to capture both the magnitude and variability of air entrainment across sea states. Finally, we demonstrate how improved sea-state-dependent  $V_a$  propagates into two applications that are sensitive to breaking-driven bubbles: bubble-mediated gas transfer velocity and sea-salt aerosol emission, highlighting differences relative to wind-only and semi-bulk parameterizations.

The paper is organized as follows. Section 2 describes the WW3 simulations, predictor construction, and the MLP training. Section 3 evaluates the parameterization globally and against HiWinGS observations and quantifies implications for bubble-mediated gas transfer and sea-salt emission. Section 4 summarizes conclusions and limitations.

## 2 Methodology

### 2.1 Numerical Modeling

The breaking-crest distribution framework  $\Lambda(c)$  is implemented in the ST4 source term of WAVEWATCH III (WW3) (Ardhuin et al., 2010). We use WW3 v7.14 in a global configuration at  $0.5^\circ$  resolution with 42 frequencies and 36 directions, following Zhou et al. (2023). The model is forced by 3-hourly 10-m neutral winds  $U_{10}$  from JRA55-do (Tsujino et al., 2018) and includes monthly varying sea ice from a coupled ocean-sea-ice simulation forced by JRA55-do fields (Adcroft et al., 2019). The resolved wavenumber range ( $k = 0.0016\text{--}4 \text{ rad m}^{-1}$ ) spans long and short wind waves and enables explicit diagno-

sis of wave-breaking statistics following Romero (2019). The wave-spectrum simulation setup and validation are described in Zhou et al. (2023).

From the simulated wave spectra  $F(k, \theta)$  we diagnose  $\Lambda(c)$  and compute air-entrainment velocity  $V_a$  using Deike et al. (2017):

$$V_a = \tilde{B} \int S(k)^{3/2} \frac{c^3}{g} \Lambda(c) dc, \quad (1)$$

where  $S(k)$  is the saturation spectrum,  $c$  is phase speed, and  $\tilde{B} = 0.1$  is a constant. The  $\Lambda(c)$  distribution is linked to the WW3 dissipation source term via the wave-breaking model of Romero (2019). We archive 3-hourly fields for 1980–2022, including  $V_a$ , significant wave height  $H_s$ , friction velocity  $u_*$ , wave age ( $c_p/U_{10}$ ), and steepness ( $k_p H_s/2$ ).

## 2.2 Neural network model and training

We train a multilayer perceptron (MLP) to predict  $V_a$  from seven physically motivated predictors:  $H_s$ ,  $U_{10}$ , wind direction ( $\cos \theta, \sin \theta$ ), wave age  $c_p/U_{10}$ , wave steepness  $k_p H_s/2$ , and water depth  $d$  (Figure 1). The MLP consists of four fully connected hidden layers with 512 neurons each and GELU activations, followed by a linear output layer. A dropout rate of 0.1 is applied in each hidden layer for regularization.

We explored alternative depths (2, 4, and 6 layers) using a reduced diagnostic dataset; two-layer models underperformed and gains beyond four layers were marginal relative to added cost, so we adopt the four-layer configuration (Table S1 in Supporting Information). The model is trained with Adam (learning rate  $10^{-3}$ , weight decay  $10^{-4}$ ) to minimize mean squared error. Training uses mixed-precision, distributed data-parallel optimization across multiple GPUs with stochastic pointwise sampling from the multi-decadal global dataset, so an epoch corresponds to a fixed number of optimization steps rather than a complete pass through the data. Training and validation losses drop rapidly within the first 8-10 epochs and remain stable (Figure S1), we therefore train the final model for 12 epochs.

We split the 1980–2022 dataset into training (1980–2014), validation (2015–2018), and testing (2019–2022), corresponding to 80%, 10%, and 10% of the samples, respectively. Predicted  $V_a$  from the MLP model was evaluated against withheld WW3 reference fields and independent HiWinGS observations (Brumer et al., 2017) using *RMSE*, bias, and correlation. The model reproduces the expected dependence of  $V_a$  on wind speed, wave age, and steepness implied by the  $\Lambda(c)$  framework and performs consistently across developing and mature sea states.

## 3 Results

In this study, we treat the wave spectral simulated global air entrainment velocity ( $V_a^{Spec}$ ) based on  $\Lambda(c)$  as the ground truth. To compare the MLP model with existing parameterizations, we consider the works of Deike et al. (2017) and Liang et al. (2017) who suggested parameterizations of  $V_a$  based on frictional velocity  $u_*$ , phase speed  $C_p$  and significant wave height  $H_s$ :

$$V_a^{Semi} = V_a(C_p, u_*, H_s) = a_1 C_p (u_*/\sqrt{gH_s})^{b_1},$$

and a simplified parameterization based on 10-meter wind speed  $U_{10}$ :

$$V_a^{U_{10}} = V_a(U_{10}) = a_2 (U_{10} - c_2)^{b_2}.$$

We use the same training dataset described in Section 2 to fit the above two relationships. The best fits obtained in this study are:  $V_a(u_*, H_s) = 2.4 \times 10^{-3} C_p (u_*/\sqrt{gH_s})^{2.48}$  and  $V_a(U_{10}) = 5.5 \times 10^{-6} (U_{10} - 2.35)^{1.05}$ . Note that in the following discussion, the units of  $V_a$  are changed from  $m/s$  to  $cm/hour$ .

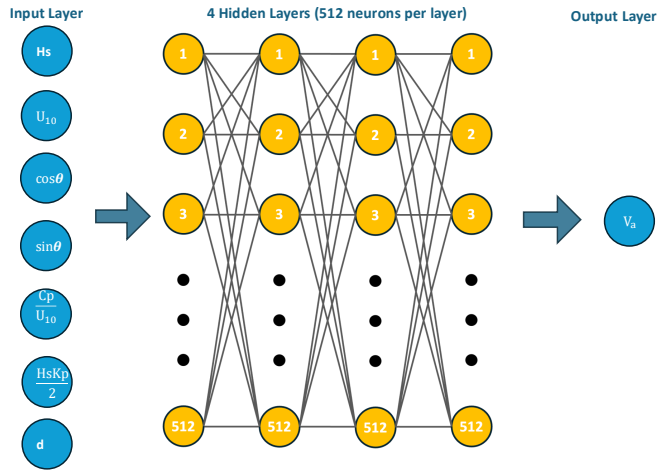


**Figure 1.** Schematic of the machine-learning framework used to parameterize the air-entrainment velocity ( $V_a$ ). Seven physically based predictors are derived from WAVEWATCH III simulations: significant wave height ( $H_s$ ), 10-m wind speed ( $U_{10}$ ), cosine and sine of wind direction ( $\cos\theta_w$ ,  $\sin\theta_w$ ), wave age ( $c_p/U_{10}$ ), wave steepness ( $k_p H_s/2$ ), and water depth ( $d$ ). These inputs are processed through a multilayer perceptron (MLP) with four hidden layers (512 neurons each, GELU activation, and 10% dropout) to predict the target variable  $V_a$ . The architecture captures nonlinear relationships between wind forcing, sea-state parameters, and air entrainment, forming the basis for a global machine-learning parameterization of wave-breaking-induced air-sea fluxes.

### 3.1 Global air entrainment from 2019 to 2022

The machine learning driven predicted  $V_a^{ML}$  shows notable improvement compared to the commonly used parameterization based on wind speed only ( $V_a^{U_{10}}$ ) and a combination of frictional velocity and significant wave height ( $V_a^{Semi}$ ) (Figure 2). Figure 2 compares the global maps of annual mean  $V_a$  for 2019–2022 derived from the three parameterizations. The reference spectral estimate  $V_a^{Spec}$  (Figure 2a) has pronounced latitudinal variability, with maxima exceeding  $40 \text{ cm h}^{-1}$  in the storm-track regions of the Southern Ocean and North Atlantic, and minima in the subtropical gyres. The machine-learning prediction  $V_a^{ML}$  (Figure 2b) closely reproduces the global spatial pattern and magnitude of  $V_a^{Spec}$ , capturing enhanced entrainment under high-wind, young-sea conditions. The semi-empirical  $V_a^{Semi}$  and wind-only  $V_a^{U_{10}}$  formulations (Figure 2c,d) show similar large-scale structure but with reduced sensitivity to regional sea-state variability. The zonal-mean comparison (Figure 2e) demonstrates that  $V_a^{ML}$  aligns best with the spectral reference, while the bulk schemes underestimate entrainment at mid to high latitudes. Difference maps (Figure 2f-h) highlight systematic biases: the ML model shows tiny residuals ( $< 0.05 \text{ cm/h}^{-1}$ ), whereas the semi-bulk and wind-based formulations underestimate  $V_a$  in storm tracks and high latitudes, while overestimate it in swell-dominated tropical regions. Overall, the ML parameterization provides a faithful and computationally efficient surrogate for the spectral model, capturing both the global distribution and zonal structure of wave-breaking-induced air entrainment.

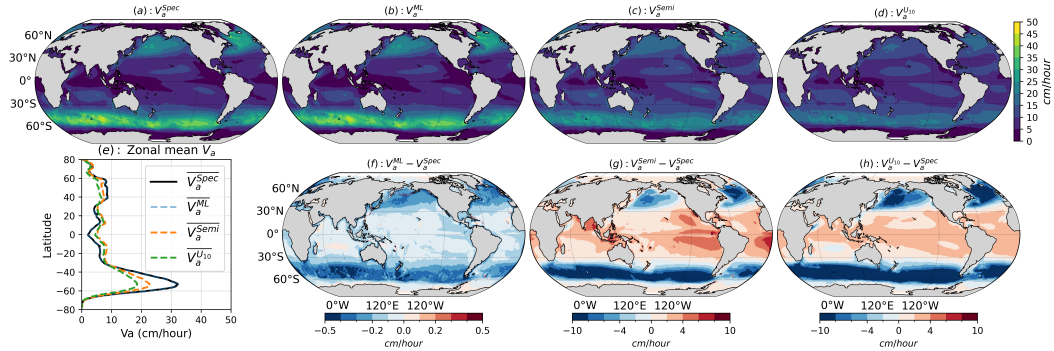


**Figure 2.** Annual mean air-entrainment velocity  $V_a$  in  $\text{cm}/\text{hour}$  from 2019–2022 for different parameterizations. Panels (a–d) show  $V_a$  computed from (a) the spectral model  $V_a^{Spec}$ , (b) the machine-learning model  $V_a^{ML}$ , (c) the semi-empirical formulation  $V_a^{Semi}$ , and (d) the wind-speed-based parameterization  $V_a^{U_{10}}$ . Panel (e) presents the zonal-mean profiles for each scheme. Panels (f–h) display spatial differences relative to the spectral reference  $V_a^{Spec}$ . The machine-learning parameterization reproduces the large-scale structure and magnitude of the spectral model while substantially reducing biases in mid-latitude storm tracks and swell-dominated regions.

Statistically, the machine-learning parameterization reproduces the spectral reference  $V_a$  with a small negative bias ( $-0.018 \text{ cm h}^{-1}$ ),  $RMSE = 0.11 \text{ cm h}^{-1}$ ,  $NRMSE = 0.08$  (normalized by the mean absolute reference), and an exceptionally high spatial correlation ( $R = 0.999$ ) over 2019–2022. In contrast, the semi-empirical formulation ( $V_a^{Semi}$ ) and the wind-only formulation ( $V_a^{U_{10}}$ ) exhibit larger systematic underestimation (biases of  $-0.081$  and  $-0.279 \text{ cm h}^{-1}$ , respectively), substantially larger errors ( $RMSE = 1.14$  and  $1.51 \text{ cm h}^{-1}$ ;  $NRMSE = 0.78$  and  $1.04$ ), and lower correlations ( $R = 0.87$  and  $0.92$ ). These results demonstrate that the ML approach captures the nonlinear dependence of air-entrainment velocity on wind forcing and sea state, substantially improving upon traditional empirical parameterizations.

### 3.2 Validation against independent observations

In addition to the 2019–2022 global simulations, the machine-learning model is evaluated against an independent observational dataset from the HiWinGS field campaign (Brumer et al., 2017), conducted aboard the R/V *Knorr* in the North Atlantic. Hourly wave statistics during HiWinGS were derived from a combination of directional wave spectra measured by the Datawell Waverider buoy and WAMOS, supplemented by a cruise-specific WAVEWATCH III (WW3) hindcast, as well as one-dimensional spectra obtained from a Riegl laser altimeter following Brumer et al. (2017). For each observation, the breaker-front distribution  $\Lambda(c)$  was estimated from the measured wave statistics and reconstructed wave spectra using the framework of Phillips (1985b) and Romero et al. (2012). The corresponding air-entrainment velocity  $V_a$  was then computed following Deike et al. (2017) and Zhou et al. (2023).

The trained model was applied to the observed sea-state variables—including significant wave height, 10-m wind speed and direction, wave age, wave steepness, and water depth—to infer  $V_a$  during the HiWinGS cruise. Figure 3 compares predicted and observed air-entrainment velocities, with symbol color indicating wave steepness  $H_s k_p/2$ . The machine-learning scheme reproduces the observed variability with a correlation coefficient of  $R = 0.76$ , an RMSE of  $64.2 \text{ cm hour}^{-1}$ , and a bias of  $53.7 \text{ cm hour}^{-1}$ , demonstrating skill for an unseen observational dataset. Predictive performance is highest under wind-driven, steep-wave conditions, whereas the model tends to overestimate air entrainment under low-wind conditions and weak wave breaking (Figure 3). In contrast, when applied to low-to-moderate wind conditions from ASIT (Hogan et al., 2025)(not shown), the model does not reproduce observed  $V_a$ . This likely reflects non-equilibrium conditions (fetch-limited and intermittent breaking) that violate the stationarity assumptions underlying the Phillips (1985)  $\Lambda(c)$  reconstruction, plus low- $c$  detection limits and potential under-resolution of weak microbreaking. These factors weaken the link between spectral saturation and  $\Lambda(c)$ , so integral formulations can misrepresent  $V_a$  outside the high-wind, near-equilibrium regime sampled by HiWinGS.

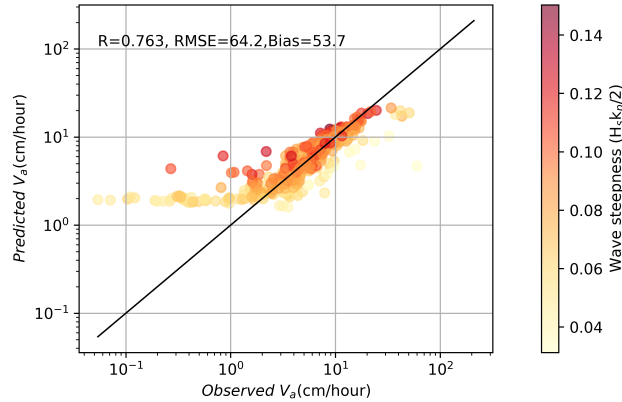


**Figure 3.** Comparison between predicted and observed air-entrainment velocity ( $V_a$ ) from the HiWinGS field campaign (Brumer et al., 2017). Colors indicate wave steepness ( $H_s k_p/2$ ).

### 3.3 Application for gas flux and sea salt emission

Since wave breaking induced bubbles impact the air-sea gas transfer velocity (Deike et al., 2017; Zhou et al., 2023) and the sea salt emission (Deike et al., 2022). We can evaluate the machine learning model presented in section 2.2 for the global application for

wave breaking induced gas transfer velocity  $k_b$  and sea salt emission due to wave breaking  $M_{salt}$ .

### 3.3.1 Global bubble mediated gas transfer velocity

Because breaking-driven bubbles influence both gas transfer velocity and sea-salt aerosol production (Deike et al., 2017; Zhou et al., 2023; Deike, 2022), we assess how the ML-based  $V_a$  affects global estimates of bubble-mediated gas transfer velocity ( $k_b$ ) and sea-salt emission. Following Zhou et al. (2023), the wave breaking induced bubbles generated gas transfer velocity  $k_b$  can be parameterized as

$$k_b = \frac{1}{2\pi\alpha} \frac{V_a}{C_A} \int \frac{4\pi R_b^3}{3} q(R_b) E(R_b) dR_b, \quad (2)$$

where  $\alpha = K_o RT$  is the Ostwald dimensionless solubility coefficient,  $K_o$  ( $mol/m^3/atm$ ) is the gas solubility in sea water,  $R$  is the ideal gas constant ( $J/K/mol$ ), and  $T$  is the sea surface skin temperature with unit  $K$ . The size distribution of bubbles entrained under a breaking wave,  $q(R_b)$ , is defined as the number of bubbles per bin size, per unit volume, follows (Deane & Stokes, 2002; Deike et al., 2022; Mostert et al., 2022)

$$q(R_b) \propto \begin{cases} R_b^{-10/3}, & R_b > R_H, \\ R_b^{-3/2}, & R_b < R_H. \end{cases} \quad (3)$$

In addition,  $E(r)$  is defined as a function of the depth of bubble injection  $z_0$  and an equilibration depth  $H_{eq}$  together with the gas diffusivity and solubility. The equilibrium depth  $H_{eq}$  is a function of the bubble rise velocity  $w_b(r)$  and the exchange velocity for a single bubble  $\kappa_b(r)$ , which depends on bubble radius  $r$ , solubility and gas diffusivity of gas in sea water. Here we use the bubble rise velocity  $w_b(r)$  in quiescent water following Keeling (1993) and Deike and Melville (2018); the details are described in Zhou et al. (2023).  $C_A$  is used to insure the volume is constrained by the third moment and dimensional consistency. In Figure 4, panel (a) shows the global zonal and monthly mean bubble-mediated gas transfer velocity  $k_b$  with increasing latitude from the spectrum simulation  $k_b^{Spec}$ , with unit  $cm/hour$ . The wave breaking induced gas transfer velocity are significant at high latitude and stronger in Boreal Winter and early spring, which is consistent with (Zhou et al., 2023; Reichl & Deike, 2020). Panels (b) to (d) in Figure 4 show the difference of zonal monthly mean bubble mediated gas transfer velocity from machine learning model and the spectrum model  $k_b^{ML} - k_b^{Spec}$ , the difference of  $k_b^{Semi}$  based on significant wave height based air entrainment reproduced gas transfer velocity and  $k_b^{Spec}$ , and the difference of gas transfer velocity from air entrainment based wind speed only  $k_b^{U_{10}}$  and  $k_b^{Spec}$ . The bias between the machine learning model and the spectrum model is in the rage of 0.1 to 0.4  $cm/hour$  or about 1% in terms of relative difference. This is a significant reduction  $O(10)$  when compared with traditional significant wave height and wind speed dependent only parameterizations.

The bubble mediated gas transfer velocity computed with the simplified parameterizations of  $V_a^{U_{10}}$  and  $V_a^{Semi}$  is overestimated in both tropical and subtropical regions due to significant wave swell signal and underestimated in the high latitude region, especially in winter seasons. The relative bias can approach  $\sim 10\%$  of the gas transfer velocity. The 10% bias of gas transfer velocity translates to a global bias of around  $15 \sim 20 PgC$  in oceanic carbon storage. The machine learning model in this study outperforms commonly used parameterizations while also being computationally efficient, qualities that are important for Earth system models.

### 3.3.2 Global sea salt emission

Deike et al. (2022) proposed a sea state dependent sea spray generation function (SSGF) based on wave breaking and bubble bursting from two mechanisms (1) film burst-

ing leading to film drops, and (2) cavity collapse leading to jet drops as following the previous studies (Lewis & Schwartz, 2004; Veron et al., 2012). The wave breaking induced SSGF is:

$$F_d(r_d) = \frac{1}{2\pi} \frac{V_a}{C_A} \int \frac{q(R_b) n(R_b)}{\langle r_d \rangle(R_b)} p\left(\frac{r_d}{\langle r_d \rangle}\right) dR_b \quad (4)$$

where the  $n(R_b)$ ,  $\langle r_d \rangle$  are respectively the number and mean radius of drops resulting from one of the mode of production (jet and film drops), the size distribution  $q(R_b)$  of bubbles entrained under a breaking waves, and defined as the number of bubbles per bin size, per unit volume, follows  $q(R_b) \propto R_b^{-10/3}$ ,  $R_b > R_H$ , while  $q(R_b) \propto R_b^{-3/2}$ ,  $R_b < R_H$  (Deane & Stokes, 2002; Deike et al., 2022; Mostert et al., 2022).

The distribution of drop size production by bubble bursting is then be modeled by a Gamma distribution  $P$  (Villermaux, 2020):

$$P(r_d / \langle r_d \rangle) = \frac{m^m}{\Gamma(m)} \left(\frac{r_d}{\langle r_d \rangle}\right)^{m-1} e^{-m \frac{r_d}{\langle r_d \rangle}}$$

with  $m = 11$ . The bubble radius in this study ranges from  $60\mu\text{m} \sim 1.2\text{mm}$  following Deike et al. (2017).

The mechanisms controlling the number and mean droplet radius produced by bubble bursting are described in detail by Deike et al. (2022); here we summarize the three modes used in this study. Jet drops form when the bubble cavity collapses and produces an upward jet that breaks into droplets. Jet drops are generated by bubbles with radius  $R_b < l_\mu$ , with  $n_{\text{jet}}(R_b) = \chi_1(R_b/l_\mu)^{-1/3}$  and  $\langle r_d \rangle_{\text{jet}} = \chi_2 l_\mu (R_b/l_\mu)^{5/4}$ , where  $\chi_1 = 145$ ,  $\chi_2 = 0.008$ , and  $l_\mu$  is the visco-capillary length.

Film drops arise from rupture of the thin liquid film separating the bubble from the atmosphere and occur in two modes Deike et al. (2022). Mode I (centrifugal ejection) applies to  $R_b \approx 0.6\text{--}10\text{ mm}$  in seawater, with  $n_{\text{filmI}}(R_b) = \chi_3(R_b/l_c)^2 (R_b/h_b)^{7/8}$  and  $\langle r_d \rangle_{\text{filmI}} = \chi_4 R_b^{3/8} h_b^{5/8}$ , where  $h_b = \chi_5 S c^{-1/2} R_b^2 / l_c$  and  $\chi_3 = 0.04$ ,  $\chi_4 = 0.5$ ,  $\chi_5 = 0.04$  (Villermaux, 2020). Mode II (flapping) applies to  $R_b \approx 100\mu\text{m}\text{--}1.2\text{ mm}$ , with  $n_{\text{filmII}}(R_b) = \chi_6 S c^{-1/2} (R_b/l_c)^2$  and  $\langle r_d \rangle_{\text{filmII}} = \chi_7 S c^{-1/2} (R_b/l_c)^{1/3}$ , where  $\chi_6 = 3.6 \times 10^6$  and  $\chi_7 = 5 \times 10^{-5}$  (Jiang et al., 2022). The total sea-spray generation function is the sum of these three contributions.

The emission of sea salt is estimated following De Leeuw et al. (2011) and Lewis and Schwartz (2004). The mass of a single particle is  $m_{\text{dry}} = \rho_{ss} 4/3\pi (r_d^{80})^3$ , where  $\rho_{ss} = 1.22\text{g/cm}^3$  is the sea salt density. Based on the sea salt generation function from Deike et al. (2022), we estimated the global sea salt emission with the diameter  $D < 10\mu\text{m}$  from the wave spectrum based air entrainment  $V_a$ , the machine learning model reproduced  $V_a^{\text{ML}}$ , the significant wave height reproduced  $V_a^{\text{Semi}}$  and the wind speed only parameterized  $V_a^{U_{10}}$ .

Figure 4 (e) shows the zonal monthly mean sea salt emission for  $D_p < 10\mu\text{m}$  from the wave spectrum model simulated  $V_a^{\text{Spec}}$ . The global pattern of sea salt emissions is similar to gas transfer velocity. This is expected, as both quantities are directly related to wave breaking. The estimated global emission with  $D < 10\mu\text{m}$  are about  $22\text{Tg/yr}$ . The machine learning model can be nearly identical with the spectrum model simulated global sea salt emission as shown in Figure 4 (f). However, both significant wave height and wind speed dependent parameterization introduce a nearly 30% bias for sea salt emission. They overestimate the emission in tropical and underestimate it at high latitude. The mechanism of such significant bias is due to the strong swell in tropical and subtropical, while the strong swell don't directly produce wave breaking as discussed in Zhou et al. (2023).

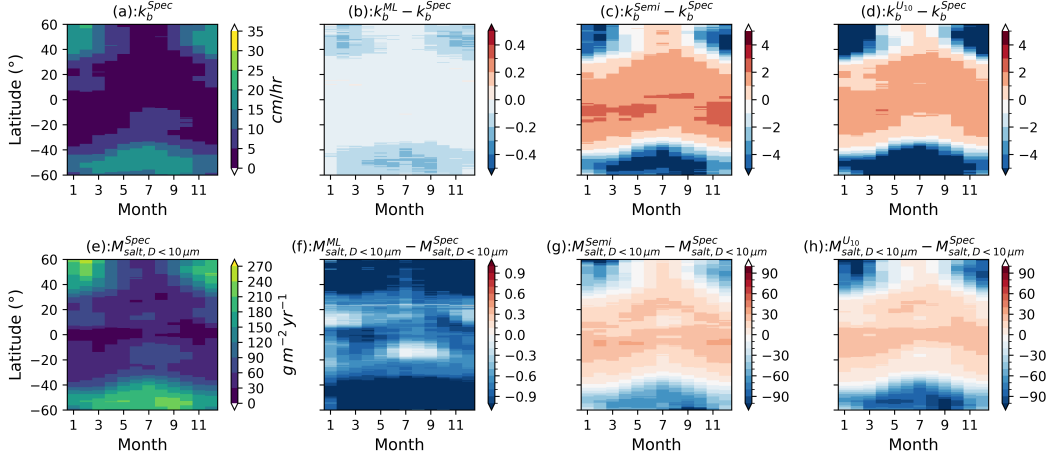


**Figure 4.** a) The global zonal monthly bubble mediated gas transfer velocity from the wave spectrum model predicted air entrainment velocity  $k_b^{spec}$  from 2019 to 2022. b) The difference of bubble mediated gas transfer velocity from air entrainment velocity based on different model, the difference between machine learning model and wave spectrum model. c) The difference between semi-bulk model based on significant wave height and wave spectrum model. d) The difference between bulk model based on wind speed only and wave spectrum model. Panels (e) to (h) similar to the previous panels, but for the sea salt emissions with droplet diameter less than  $10\mu\text{m}$ .

#### 4 Conclusions and discussion

We developed an MLP-based parameterization of wave-breaking air-entrainment velocity  $V_a$ , a key quantity controlling bubble-mediated air-sea exchange. The work is motivated by the computational cost of diagnosing  $V_a$  from a full spectral model with  $\Lambda(c)$ , and by systematic regional biases in commonly used wind-only and semi-bulk formulations. The ML model reproduces the spectral-reference  $V_a$  globally and shows skill against independent HiWinGS observations. When propagated into applications, the ML-based  $V_a$  substantially reduces regional biases in bubble-mediated gas transfer velocity and sea-salt emissions relative to traditional parameterizations.

This framework is currently limited by the Phillips (1985) equilibrium-breaking assumption and is most reliable under deep-water, near-equilibrium conditions. As additional observations become available—particularly in shallow-water and non-equilibrium regimes—the approach can be extended by retraining with expanded training targets. Overall, the parameterization provides an efficient pathway to improve sea-state-dependent air-sea flux representations in Earth system models.

#### Open Research Section

WAVEWATCH III is publicly available (<https://github.com/NOAA-EMC/WW3>). The implementation of the breaking-crest distribution  $\Lambda(c)$  in WWIII, following (Romero, 2019), is available at <https://github.com/Leonel-Romero/WW3-Lambda>. For peer review, the wave-spectral simulation outputs used in this study, the machine-learning predictions, and the trained machine-learning model (weights and configuration) are available at <https://utdallas.app.box.com/v/zhou-jgr-2026>. HiWinGS cruise data products used for validation are publicly available via the NOAA PSL cruise archive <https://psl.noaa.gov/data/cruises/>.

## Conflict of Interest declaration

The authors declare there are no conflicts of interest for this manuscript.

## Acknowledgments

This research was supported by the NASA Modeling, Analysis, and Prediction (MAP) Program through the Global Modeling and Assimilation Office: Core Activities, and by the National Science Foundation (NSF) under grant number 2319535. Any opinions, findings, and conclusions or recommendations expressed in this material are those of the authors and do not necessarily reflect the views of NSF. The computational resources were provided by NOAA's RDHPC systems, Texas Advanced Computing Center (TACC) at the University of Texas at Austin through allocations OCE24006 and OCE24007, and Purdue Anvil CPU at Purdue University through allocation PHY240204 from the Advanced Cyberinfrastructure Coordination Ecosystem: Services & Support (ACCESS) program.

## References

Adcroft, A., Anderson, W., Balaji, V., Blanton, C., Bushuk, M., Dufour, C. O., ... others (2019). The gfdl global ocean and sea ice model om4. 0: Model description and simulation features. *Journal of Advances in Modeling Earth Systems*, 11(10), 3167–3211.

Ardhuin, F., Rogers, E., Babanin, A. V., Filipo, J.-F., Magne, R., Roland, A., ... others (2010). Semiempirical dissipation source functions for ocean waves. part i: Definition, calibration, and validation. *Journal of Physical Oceanography*, 40(9), 1917–1941.

Banner, M. L., & Peirson, W. L. (2000). Wave breaking onset and strength for two-dimensional deep water wave groups. *Journal of Fluid Mechanics*, 464, 133–153. doi: 10.1017/S0022112000008296

Brumer, S., Zappa, C. J., Tremblay, J. E., & Papakyriakou, T. (2017). Whitecap coverage dependence on wind speed and solar irradiance in the arctic ocean. *Geophysical Research Letters*, 44(1), 279–285. doi: 10.1002/2016GL071471

Callaghan, A. H., Deane, G. B., Stokes, M. D., & Ward, B. (2012). Observed variation in the decay time of oceanic whitecap foam. *Journal of Geophysical Research: Oceans*, 117(C9).

Callaghan, A. H., & White, M. (2008). Automated processing of sea surface images for the determination of whitecap coverage. *Journal of Atmospheric and Oceanic Technology*, 26(2), 383–394. doi: 10.1175/2007JTECHO586.1

Dakar, E., Fernández Jaramillo, J. M., Gertman, I., Mayerle, R., & Goldman, R. (2023). An artificial neural network based system for wave height prediction. *Coastal Engineering Journal*, 1–16.

Deane, G. B., & Stokes, M. D. (2002). Scale dependence of bubble creation mechanisms in breaking waves. *Nature*, 418(6900), 839–844.

Deike, L. (2022). Mass transfer at the ocean–atmosphere interface: the role of wave breaking, droplets, and bubbles. *Annual Review of Fluid Mechanics*, 54(1), 191–224.

Deike, L., & Melville, W. K. (2018). Gas transfer by breaking waves. *Geophysical Research Letters*, 45(19), 10–482.

Deike, L., Melville, W. K., & Popinet, S. (2017). Air entrainment and bubble statistics in breaking waves. *Journal of Fluid Mechanics*, 801, 91–129.

Deike, L., Reichl, B., & Paulot, F. (2022). A mechanistic sea spray generation function based on the sea state and the physics of bubble bursting. *AGU Advances*, 3(6), e2022AV000750.

Deike, L., Zhou, X., Rustogi, P., Stanley, R. H., Reichl, B. G., Bushinsky, S. M., & Resplandy, L. (2025). A universal wind–wave–bubble formulation for air–sea

gas exchange and its impact on oxygen fluxes. *Proceedings of the National Academy of Sciences*, 122(38), e2419319122.

De Leeuw, G., Andreas, E. L., Anguelova, M. D., Fairall, C., Lewis, E. R., O'Dowd, C., ... Schwartz, S. E. (2011). Production flux of sea spray aerosol. *Reviews of Geophysics*, 49(2).

Di Giorgio, S., Pirozzoli, S., & Iafrati, A. (2025). Air entrainment and gas transfer in wave breaking events. *Geophysical Research Letters*, 52(15), e2025GL114907.

Hogan, L., Zappa, C. J., Cifuentes-Lorenzen, A., Edson, J. B., O'Donnell, J., & Ullman, D. S. (2025). Observations of breaking wave dissipation and their relationship to atmosphere-ocean energy transfer. *Journal of Geophysical Research: Oceans*, 130(6), e2024JC022130.

James, S. C., Zhang, Y., & O'Donncha, F. (2018). A machine learning framework to forecast wave conditions. *Coastal Engineering*, 137, 1–10.

Jiang, X., Rotily, L., Villermaux, E., & Wang, X. (2022). Submicron drops from flapping bursting bubbles. *Proceedings of the National Academy of Sciences*, 119(1), e2112924119.

Keeling, R. F. (1993). On the role of large bubbles in air-sea gas exchange and supersaturation in the ocean.

Lewis, E. R., & Schwartz, S. E. (2004). *Sea salt aerosol production: mechanisms, methods, measurements, and models* (Vol. 152). American Geophysical Union.

Liang, J. H., Reichl, B. G., Fox-Kemper, B., Sullivan, P. P., & McWilliams, J. C. (2017). Parameterizing turbulent langmuir mixing using large-eddy simulations: Tests with advection–diffusion and buoyancy forcing. *Journal of Physical Oceanography*, 47(12), 3061–3087. doi: 10.1175/JPO-D-17-0079.1

Lou, R., Lv, Z., Dang, S., Su, T., & Li, X. (2021). Application of machine learning in ocean data. *Multimedia Systems*, 1–10.

Melville, W. K. (1996). The role of surface-wave breaking in air-sea interaction. *Annual Review of Fluid Mechanics*, 28, 279–321. doi: 10.1146/annurev.fl.28.010196.001431

Melville, W. K. (2016). The dynamics of breaking waves. *Annual Review of Fluid Mechanics*, 48, 379–409. doi: 10.1146/annurev-fluid-122414-034212

Mostert, W., Popinet, S., & Deike, L. (2022). High-resolution direct simulation of deep water breaking waves: transition to turbulence, bubbles and droplets production. *Journal of Fluid Mechanics*, 942, A27.

O'Donncha, F., Zhang, Y., Chen, B., & James, S. C. (2018). An integrated framework that combines machine learning and numerical models to improve wave-condition forecasts. *Journal of Marine Systems*, 186, 29–36.

O'Donncha, F., Zhang, Y., Chen, B., & James, S. C. (2019). Ensemble model aggregation using a computationally lightweight machine-learning model to forecast ocean waves. *Journal of Marine Systems*, 199, 103206.

Peláez-Zapata, D., Pakrashi, V., & Dias, F. (2024). Dynamics of bubble plumes produced by breaking waves. *Journal of Physical Oceanography*, 54(10), 2059–2071.

Phillips, O. M. (1985a). Spectral and statistical properties of the equilibrium range in wind-generated gravity waves. *Journal of Fluid Mechanics*, 156, 505–531.

Phillips, O. M. (1985b). Spectral and statistical properties of the equilibrium range in wind-generated gravity waves. *Journal of Fluid Mechanics*, 156, 505–531.

Reichl, B. G., & Deike, L. (2020). Contribution of sea-state dependent bubbles to air-sea carbon dioxide fluxes. *Geophysical Research Letters*, 47(9), e2020GL087267.

Romero, L. (2019). Distribution of surface wave breaking fronts. *Geophysical Research Letters*, 46(17–18), 10463–10474.

Romero, L., Melville, W. K., & Kleiss, J. M. (2012). Spectral energy dissipation due to surface wave breaking. *Journal of Physical Oceanography*, 42(9), 1421–1444.

doi: 10.1175/JPO-D-11-072.1

Ruth, D. J., Néel, B., Erinin, M. A., Mazzatorta, M., Jaquette, R., Veron, F., & Deike, L. (2022). Three-dimensional measurements of air entrainment and enhanced bubble transport during wave breaking. *Geophysical Research Letters*, 49(16), e2022GL099436.

Sun, D., Huang, W., Luo, Y., Luo, J., Wright, J. S., Fu, H., & Wang, B. (2022). A deep learning-based bias correction method for predicting ocean surface waves in the northwest pacific ocean. *Geophysical Research Letters*, 49(23), e2022GL100916. doi: <https://doi.org/10.1029/2022GL100916>

Sutherland, P., & Melville, W. K. (2016). Field measurements and scaling of ocean-surface wave-breaking statistics. *Geophysical Research Letters*, 43(3), 1221–1228. doi: 10.1002/2015GL067490

Thorpe, S. A. (1995). Dynamical processes of transfer at the sea surface. *Progress in Oceanography*, 35, 315–352.

Tsujino, H., Urakawa, S., Nakano, H., Small, R. J., Kim, W. M., Yeager, S. G., ... others (2018). Jra-55 based surface dataset for driving ocean-sea-ice models (jra55-do). *Ocean Modelling*, 130, 79–139.

Veron, F., Hopkins, C., Harrison, E., & Mueller, J. (2012). Sea spray spume droplet production in high wind speeds. *Geophysical Research Letters*, 39(16).

Villermaux, E. (2020). Fragmentation versus cohesion. *Journal of Fluid Mechanics*, 898, P1.

Xu, G., Zhang, S., & Shi, W. (2023). Instantaneous prediction of irregular ocean surface wave based on deep learning. *Ocean Engineering*, 267, 113218.

Zhang, J., Zhao, X., Jin, S., & Greaves, D. (2022). Phase-resolved real-time ocean wave prediction with quantified uncertainty based on variational bayesian machine learning. *Applied Energy*, 324, 119711.

Zhou, X., Reichl, B. G., Romero, L., & Deike, L. (2023). A sea state dependent gas transfer velocity for co2 unifying theory, model, and field data. *Earth and Space Science*, 10(11), e2023EA003237.